SOLAR CELLS

A mixed-cation lead mixed-halide perovskite absorber for tandem solar cells

David P. McMeekin,[1] Golnaz Sadoughi,[1] Waqaas Rehman,[1] Giles E. Eperon,[1] Michael Saliba,[1] Maximilian T. Hörantner,[1] Amir Haghighirad,[1] Nobuya Sakai,[1] Lars Korte,[2] Bernd Rech,[2] Michael B. Johnston,[1] Laura M. Herz,[1] Henry J. Snaith[1]*

Metal halide perovskite photovoltaic cells could potentially boost the efficiency of commercial silicon photovoltaic modules from ~20 toward 30% when used in tandem architectures. An optimum perovskite cell optical band gap of ~1.75 electron volts (eV) can be achieved by varying halide composition, but to date, such materials have had poor photostability and thermal stability. Here we present a highly crystalline and compositionally photostable material, $[HC(NH_2)_2]_{0.83}Cs_{0.17}Pb(I_{0.6}Br_{0.4})_3$, with an optical band gap of ~1.74 eV, and we fabricated perovskite cells that reached open-circuit voltages of 1.2 volts and power conversion efficiency of over 17% on small areas and 14.7% on 0.715 cm^2 cells. By combining these perovskite cells with a 19%-efficient silicon cell, we demonstrated the feasibility of achieving >25%-efficient four-terminal tandem cells.

One concept for improving the efficiency of photovoltaics (PVs) is to create a "tandem junction"; for example, by placing a wide–band-gap "top cell" above a silicon (Si) "bottom cell." This approach could realistically increase the efficiency of the Si cell from 25.6 to beyond 30% (*1*, *2*). Given the crystalline Si band gap of 1.1 eV, the top cell material requires a band gap of ~1.75 eV in order to current-match both junctions (*3*). However, suitable wide–band-gap top-cell materials for Si or thin-film technologies that offer stability, high performance, and low cost have been lacking. In recent years, metal halide perovskite–based PVs have gained attention because of their high power conversion efficiencies (PCEs) and low processing cost (*4*–*11*). An attractive feature of this material is the ability to tune its band gap from 1.48 to 2.3 eV (*12*, *13*), implying that we could potentially fabricate an ideal material for tandem cell applications.

Perovskite-based PVs are generally fabricated with organic-inorganic trihalide perovskites with the formulation ABX_3, where A is the methylammonium (CH_3NH_3) (MA) or formamidinium ($HC(NH_2)_2$) (FA) cation, B is commonly lead (Pb), and X is a halide (Cl, Br, or I). Although these perovskite structures offer high PCEs, reaching >20% PCE with band gaps of around 1.55 eV (*14*), fundamental issues have been discovered when attempting to tune their band gaps to the optimum 1.7- to 1.8-eV range. In the case of $MAPb[I_{(1-x)}Br_x]_3$, Hoke *et al.* reported that soaking it with light induces a halide segregation within the perovskite (*15*). The formation of iodide-rich domains with a lower band gap results in an increase in sub-gap absorption and a red shift of photoluminescence (PL). The lower–band-gap regions limit the voltage attainable with such a material, so this band-gap "photoinstability" limits the use of $MAPb[I_{(1-x)}Br_x]_3$ in tandem devices (*15*). In addition, when considering real-world applications, $MAPbI_3$ is inherently thermally unstable at temperatures above 85°C, even in aninert atmosphere (international regulations require a commercial PV product to withstand this temperature) (*16*).

Concerning the more thermally stable $FAPbX_3$ perovskite, an increase in optical band gap has

[1]Clarendon Laboratory, University of Oxford, Parks Road, Oxford OX1 3PU, UK. [2]Helmholtz-Zentrum Berlin für Materialien und Energie, Institute for Silicon Photovoltaics, Kekuléstrasse 5, 12489 Berlin, Germany.
*Corresponding author. E-mail: henry.snaith@physics.ox.ac.uk

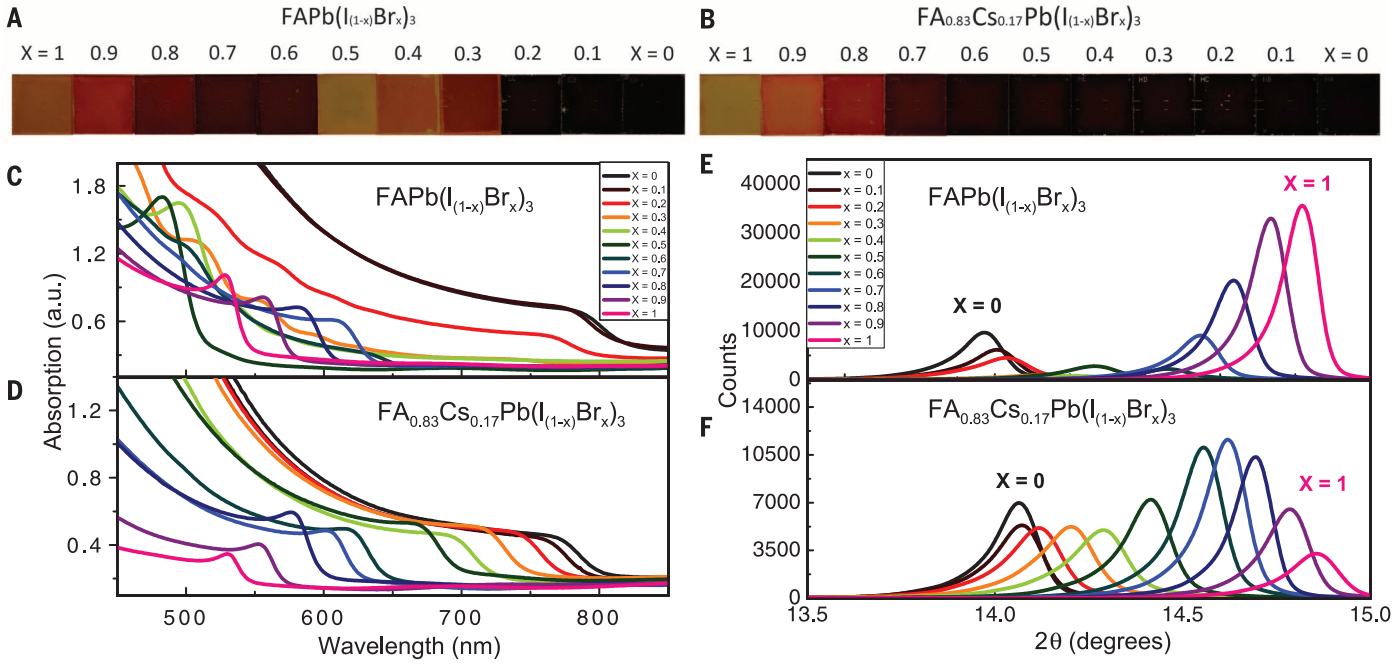

Fig. 1. Tuning the band gap. Photographs of perovskite films with Br composition increasing from $x = 0$ to 1 for (**A**) $FAPb[I_{(1-x)}Br_x]_3$ and (**B**) $FA_{0.83}Cs_{0.17}Pb[I_{(1-x)}Br_x]_3$. (**C**) Ultraviolet-visible absorbance spectra of films of $FAPb[I_{(1-x)}Br_x]_3$ and (**D**) $FA_{0.83}Cs_{0.17}Pb[I_{(1-x)}Br_x]_3$. a.u., arbitrary units. (**E**) XRD pattern of $FAPb[I_{(1-x)}Br_x]_3$ and (**F**) $FA_{0.83}Cs_{0.17}Pb[I_{(1-x)}Br_x]_3$. The stated compositions are the fractional compositions of the ions in the starting solution, and the actual composition of the crystallized films may vary slightly.

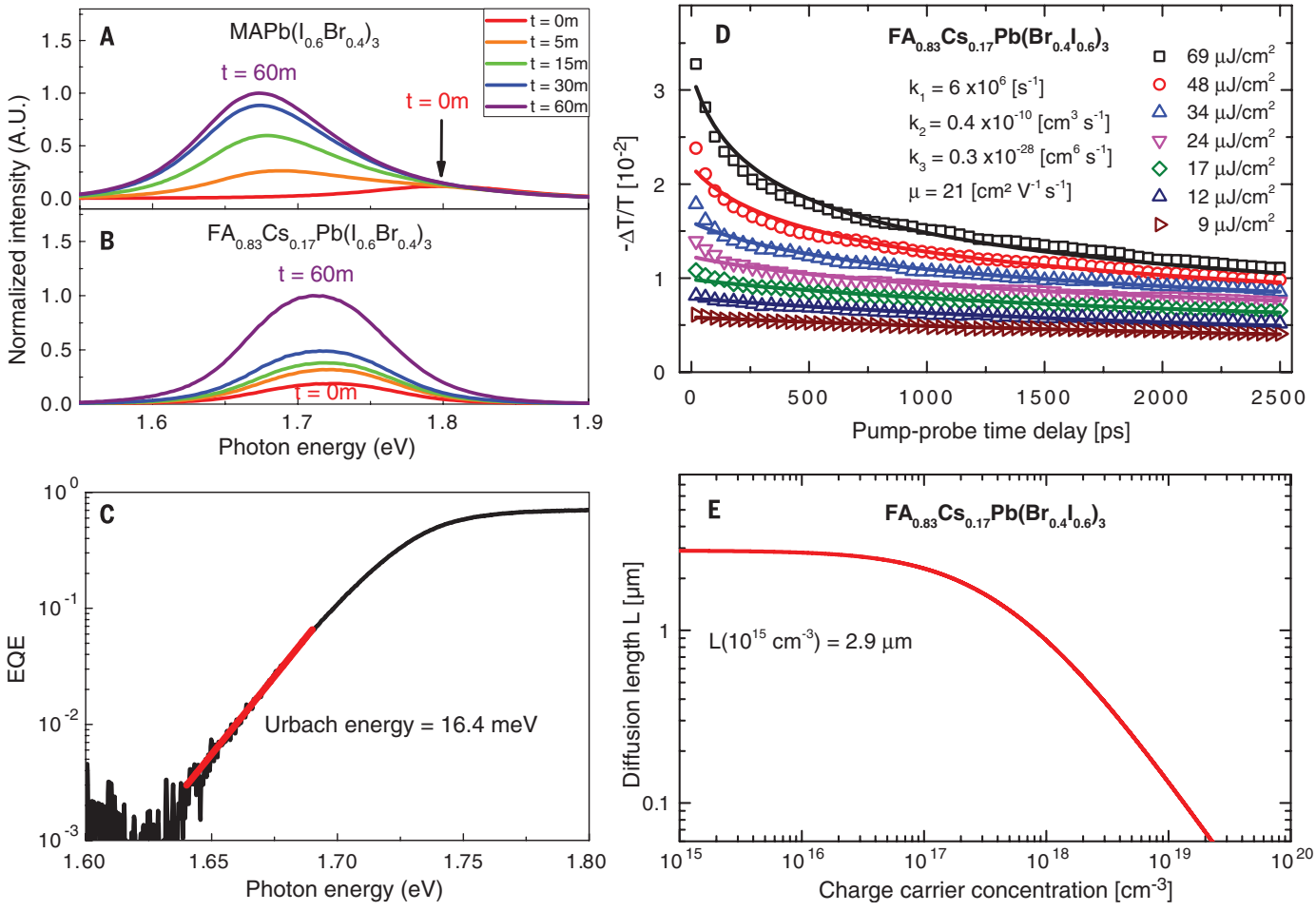

Fig. 2. Material characteristics of $FA_{0.83}Cs_{0.17}Pb(I_{0.6}Br_{0.4})_3$ perovskite. Normalized PL measurement measured after 0, 5, 15, 30, and 60 min of light exposure of the (**A**) $MAPb(I_{0.6}Br_{0.4})_3$ and (**B**) $FA_{0.83}Cs_{0.17}Pb(I_{0.6}Br_{0.4})_3$ thin films. (**C**) Semi-log plot of EQE at the absorption onset for a $FA_{0.83}Cs_{0.17}Pb(I_{0.6}Br_{0.4})_3$ PV cell, measured using FTPS at short-circuit (J_{SC}). (**D**) OPTP transients for a $FA_{0.83}Cs_{0.17}Pb(I_{0.6}Br_{0.4})_3$ thin film, measured after excitation with a 35-fs light pulse of wavelength 400 nm with different fluences. (**E**) Charge-carrier diffusion length L as a function of charge-carrier concentration.

not resulted in an expected increase in open-circuit voltage (V_{OC}) (*13*). Furthermore, as iodide is substituted with bromide, a crystal phase transition occurs from a trigonal to a cubic structure; in compositions near the transition, the material is unable to crystallize, resulting in an apparently "amorphous" phase with high levels of energetic disorder and unexpectedly low absorption. These compositions additionally have much lower charge-carrier mobilities in the range of 1 $cm^2 V^{-1} s^{-1}$, in comparison to >20 $cm^2 V^{-1} s^{-1}$ in the neat iodide perovskite (*17*). For tandem applications, these problems arise at the Br composition needed to form the desired top-cell band gap of ~1.7 to 1.8 eV.

Nevertheless, perovskite/Si tandem PVs have already been reported in four-terminal (*18*, *19*) and two-terminal (*20*) architectures. However, their reported efficiencies have yet to surpass the optimized single-junction efficiencies, in part because of non-ideal absorber band gaps. It is possible to form a lower–band-gap triiodide perovskite material and current-match the top and bottom junctions in a monolithic architecture by simply reducing the thickness of the top cell. However, this method results in non-ideal efficiency.

Here we address the issues of forming a photostable FA-based perovskite with the ideal band gap for tandem PVs. We partially substituted the formamidinium cation with Cs and observed that the phase instability region was entirely eliminated in the iodide-to-bromide compositional range, delivering complete tunability of the band gap around 1.75 eV. We fabricated planar heterojunction perovskite PVs, demonstrating PCE of >17% and stabilized power output (SPO) of 16%. To demonstrate the potential impact of this new perovskite material in tandem solar cells, we created a semi-transparent perovskite device and measured the performance of a silicon PV after "filtering" the sunlight through the perovskite top cell. The Si cells delivered an efficiency boost of 7.3%, indicating the feasibility of achieving >25%-efficient perovskite/Si tandem cells.

The A-site cations that could be used with lead halides to form suitable perovskites for PVs are Cs, MA, and FA. $CsPbI_3$ does form a "black phase" perovskite with a band gap of 1.73 eV, but this appropriate phase is only stable at temperatures above 200° to 300°C, and the most stable phase at room temperature is a nonperovskite orthorhombic "yellow" phase. MA-based perovskites are thermally unstable and suffer from halide segregation instabilities, and are thus likely to be unsuitable (*16*). FA-based perovskites are the most likely to deliver the best balance between structural and thermal stability (*13*, *21*–*25*). However, in Fig. 1A, we show photographs of a series of $FAPb[I_{(1-x)}Br_x]_3$ films; we observed a "yellowing" of the films for compositions of x between 0.3 and 0.6, which is consistent with the previously reported phase instability caused by a transition from a trigonal ($x < 0.3$) to a cubic ($x > 0.5$) structure (*13*).

We have previously observed that the band gap changes from 1.48 eV for $FAPbI_3$ to 1.73 eV for $CsPbI_3$ (*13*). Recently it has been shown that mixing Cs with FA or MA results in a slight widening of the band gap (*26*, *27*). We considered the possibility that if we partially substituted FA for Cs, we could push this region of structural instability in the Br-to-I phase space to higher energies, and thus potentially achieve a structurally stable mixed-halide perovskite with a band gap of 1.75 eV. In Fig. 1B, we show photographs of thin films fabricated from mixed-cation lead mixed-halide $FA_{0.83}Cs_{0.17}Pb[I_{(1-x)}Br_x]_3$ compositions.

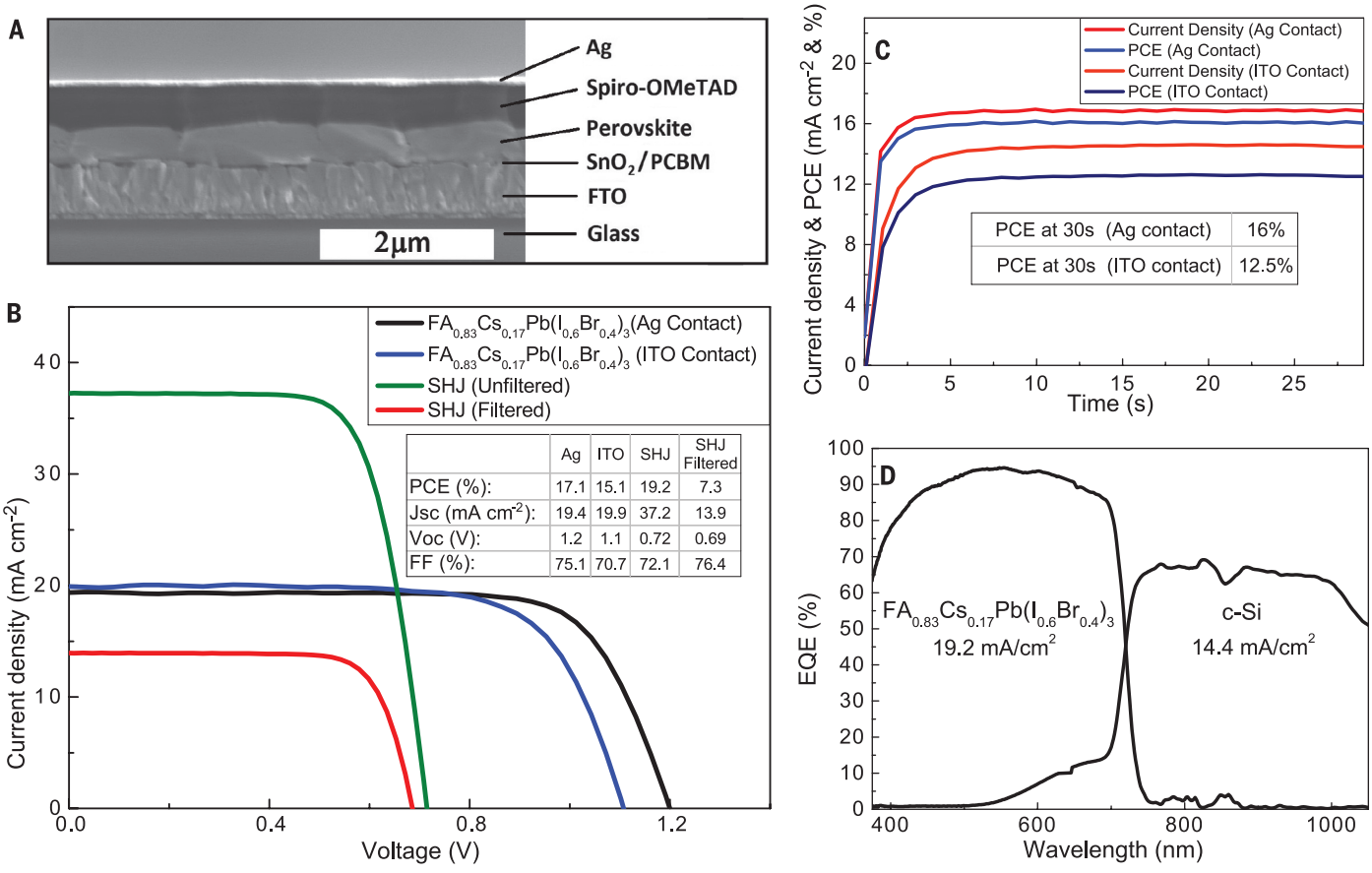

Fig. 3. Device architecture and *I-V* characteristics for $FA_{0.83}Cs_{0.17}Pb(I_{0.6}Br_{0.4})_3$ perovskite and Si PV cells. (**A**) Scanning electron microscope image of a cross-section of a planar heterojunction solar cell. PCBM, phenyl-C60-butyric acid methyl ester. (**B**) Forward bias to short-circuit *I-V* curve for the best perovskite devices fabricated, using either a Ag metal or semi-transparent ITO top electrode, measured at a 0.38 V/s scan rate. FF, fill factor. We also show the *I-V* curve of a SHJ cell, measured with direct light or with the simulated sunlight filtered through the semi-transparent perovskite solar cell (*37*). The SHJ cells were measured at the Centre For Renewable Energy Technologies, Loughborough, UK, under an extremely well-calibrated solar simulator. (**C**) Photocurrent density and power conversion efficiency measured at the maximum power point for a 30-s time span. (**D**) EQE spectrum measured in short-circuit (J_{SC}) configuration for the highest-efficiency perovskite cell and the SHJ cell measured with the incident light filtered through the semi-transparent perovskite cell.

Unexpectedly, we did not simply shift the region of structural instability to higher energy, but we observed a continuous series of dark films throughout this entire compositional range. To confirm these observations, we also performed ultraviolet-visible absorption measurements. We obtained a sharp optical band edge for all compositions of the $FA_{0.83}Cs_{0.17}Pb[I_{(1-x)}Br_x]_3$ material (Fig. 1, C and D), in contrast to $FAPb[I_{(1-x)}Br_x]_3$, which shows weak absorption in the intermediate range.

In order to understand the impact of adding Cs upon the crystallization of the perovskite, we performed x-ray diffraction (XRD) on the series of films covering the I-to-Br compositional range. In Fig. 1E, we show the XRD patterns for $FAPb[I_{(1-x)}Br_x]_3$, zoomed in to the peak around 2θ ~ 14° [the complete diffraction pattern is shown in fig. S1, along with more details on fitting these data (*28*)]. For the $FA_{0.83}Cs_{0.17}Pb[I_{(1-x)}Br_x]_3$ perovskite, the material is in a single phase throughout the entire composition range. The monotonic shift of the (100) reflection that we observed from 2θ ~ 14.2° to 14.9° is consistent with a shift of the cubic lattice constant from 6.306 to 5.955 Å as the material incorporates a larger fraction of the smaller halide, Br [in fig. S2, we show the complete diffraction pattern (*28*)]. Thus, for the $FA_{0.83}Cs_{0.17}Pb[I_{(1-x)}Br_x]_3$ perovskite, we have removed the structural phase transition and instability over the entire compositional range [in figs. S3 to S5 we show details of varying the Cs concentration and the Br-to-I concentration (*28*)]. Over the entire Br-to-I range, and for a large fraction of the Cs-FA range, the variation in lattice constant, composition, and optical band gap precisely follows Vegard's law [fig. S6 (*28*)], so we have total flexibility and predictability in tuning the composition and its impact on the band gap. For the results that follow below, we used the precise composition $FA_{0.83}Cs_{0.17}Pb(I_{0.6}Br_{0.4})_3$, which has an optical band gap of 1.74 eV as determined by a Tauc plot [fig. S7 (*28*)].

Photoinduced halide segregation has been reported in methylammonium lead mixed-halide perovskites (*15*). A red shift in PL upon light illumination, for intensities ranging from 10 to 100 mW cm^{-2} occurs, with the shift to lower energies resulting from the formation of iodine-rich domains that have lower band gaps. This limits the achievable open-circuit voltage of the solar cell device by introducing a large degree of electronic disorder. In Fig. 2, we show the PL from films of $MAPb(I_{0.6}Br_{0.4})_3$ perovskite and the mixed-cation mixed-halide material $FA_{0.83}Cs_{0.17}Pb(I_{0.6}Br_{0.4})_3$, immediately after prolonged periods of light exposure, using a power density of ~3 mW cm^{-2} and a wavelength of 550 nm as an excitation source. We confirmed the results observed by Hoke *et al.*; that is, we saw a time-dependent red shift in PL for the $MAPb(I_{0.6}Br_{0.4})_3$ film, which exhibited a 130-meV PL red shift after only 1 hour of illumination. We also show the time evolution of the PL from $MAPb(I_{0.8}Br_{0.2})_3$, a composition previously reported in other devices (*29*), which shifts from 1.72 to 1.69 eV [fig. S8 (*28*)]. In contrast, although we saw a rise in PL intensity, we observed no significant red shift in PL emission for the $FA_{0.83}Cs_{0.17}Pb(I_{0.6}Br_{0.4})_3$ precursor after 1 hour of identical light illumination (which we show in Fig. 2B). Furthermore, we exposed a similar $FA_{0.83}Cs_{0.17}Pb(I_{0.6}Br_{0.4})_3$ film to monochromatic irradiance of much higher irradiance of 5 W cm^{-2} and observed no red shift after 240 s of illumination [fig. S9, (*28*)]. Under these identical conditions, we did observe a red shift in the PL for the single-cation

$FAPb(I_{0.6}Br_{0.4})_3$ perovskite, as we have previously reported (*17*). In addition, under thermal stressing at 130°C, we observed that the optical band gap and the crystal lattice of $FA_{0.83}Cs_{0.17}Pb(I_{0.6}Br_{0.4})$ were stable, in contrast to those of $MAPb(I_{0.6}Br_{0.4})_3$ (fig. S10).

Beyond halide segregation, a further deleterious observation previously made for mixed-halide perovskites has been that the energetic disorder in the material is greatly increased in comparison to the neat iodide perovskites. The ultimate open-circuit voltage that a solar cell material can generate is intimately linked to the steepness of the absorption onset just below the band edge, which can be quantified by the Urbach energy (E_u) (*30*, *31*). This E_u reported by De Wolf *et al.* and Sadhanala *et al.* for $MAPbI_3$ was 15 meV (*31*), where small values of E_u indicate low levels of electronic disorder. In contrast, the E_u for $MAPb(I_{0.6}Br_{0.4})_3$ perovskite increased to 49.5 meV (*32*). We determined E_u by performing Fourier-transform photocurrent spectroscopy (FTPS) on complete planar heterojunction solar cells (details of the solar cells are discussed below), and in Fig. 2C we show the semi-log plot of external quantum efficiency (EQE) absorption edge of a device fabricated with the optimized precursor solution and annealing procedure. We calculated an E_u of 16.5 meV, which is near the values reported for the neat iodide perovskites.

In order to further assess the electronic quantity of $FA_{0.83}Cs_{0.17}Pb(I_{0.6}Br_{0.4})_3$, we performed optical pump terahertz-probe (OPTP) spectroscopy, which is a noncontact method of probing the photo-induced conductivity and effective charge-carrier mobility in the material. In Fig. 2D, we show the fluence dependence of the OPTP transients, which exhibit accelerated decay dynamics at higher initial photoinjected charge-carrier densities, as the result of enhanced contributions from bimolecular and Auger recombination. We extract the rate constants associated with different recombination mechanisms by global fits to these transient of the solutions to the rate equation

$$\frac{dn(t)}{dt} = -k_3 n^3 - k_2 n^2 - k_1 n \qquad (1)$$

which we show in Fig. 2D. In addition, we found that $FA_{0.83}Cs_{0.17}Pb(I_{0.6}Br_{0.4})_3$ exhibits an excellent charge-carrier mobility of 21 $cm^2\ V^{-1}\ s^{-1}$. For comparison, the corresponding neat FA perovskite $FAPb(I_{0.6}Br_{0.4})_3$ only sustains charge-carrier mobilities <1 $cm^2\ V^{-1}\ s^{-1}$ that are related to the amorphous and energetically disordered nature of these materials (*17*). Conversely, $FA_{0.83}Cs_{0.17}Pb(I_{0.6}Br_{0.4})_3$ displays a mobility value intermediate to those we previously determined (*17*) for $FAPbI_3$ (27 $cm^2\ V^{-1}\ s^{-1}$) and $FAPbBr_3$ (14 $cm^2\ V^{-1}\ s^{-1}$), which suggests that it is no longer limited by structural disorder.

We further assessed the potential of $FA_{0.83}Cs_{0.17}Pb(I_{0.6}Br_{0.4})_3$ for incorporation into planar heterojunction PV architectures by deriving the charge-carrier diffusion length $L = [\mu k_B T/(eR)]^{0.5}$ as function of the charge-carrier density n, where $R = k_1 + nk_2 + n^2k_3$ is the total recombination rate, k_B is the Boltzmann constant, T is temperature, and e is the elementary charge. In Fig. 2E, we show that for charge-carrier densities typical under solar illumination ($n \sim 10^{15}$ cm^{-3}) a value of $L \sim 2.9$ μm is reached, which is comparable to values reported for high-quality thin films of neat lead iodide perovskites (*17*, *33*). The high charge-carrier mobility, slow recombination kinetics, and the long charge carrier diffusion length imply that this mixed-cation, mixed-halide perovskite should be just as effective as a high-quality solar cell absorber material as the neat halide perovskite $FAPbI_3$.

We fabricated a series of planar heterojunction solar cells to assess the overall solar cell performance [in fig. S11 we describe in more detail and show data for solar cells fabricated with a range of compositional and processing parameters (*28*)]. We show the device architecture in Fig. 3A, which is composed of a SnO_2/phenyl-C_{60}-butyric acid methyl ester ($PC_{60}BM$) electron-selective layer, a solid $FA_{0.83}Cs_{0.17}Pb(I_{0.6}Br_{0.4})_3$ perovskite absorber layer, and Li-TFSI–doped [TFSI, bis(trifluoromethanesulfonyl)imide] spiro-OMeTAD [2,2′,7,7′-tetrakis(*N*,*N*-di-p-methoxyphenylamine)-9,9′-spirobifluorene] with 4-tert-butylpyridine (TBP) additive as the hole-collection layer, capped with an Ag electrode. We measured current-voltage (*I-V*) characteristics of such devices under a simulated air mass (AM) 1.5, under 100 mW cm^{-2} of sunlight, and show the *I-V* characteristics of one of the highest-performing devices in Fig. 3B. It delivered a short-circuit current density of 19.4 mA cm^{-2}, a V_{OC} of 1.2 V, and a PCE of 17.1%. By holding the cell at a fixed maximum power point forward-bias voltage of 0.95 V, we measured the power output over time, reaching a stabilized efficiency of 16% (Fig. 3C). The highest *I-V* scanned efficiency we measured was 17.9% [fig. S12 (*28*), along with a histogram of performance parameters for a large batch of devices in fig. S13 (*28*)]. To demonstrate that these cells can also operate with larger area, we fabricated 0.715-cm^2 active layers in which the cells reach a stabilized power output of >14% [fig. S14 (*28*)]. In Fig. 3D, we show the spectral response of the solar cell, which confirms the wider band gap of the solar cell and also integrates over the AM 1.5 solar spectrum to give 19.2 mA cm^{-2}, in close agreement to the measured short-circuit current density (J_{SC}).

This performance is very competitive with that of the best reported single-junction perovskite solar cell reported so far (*30*, *34*), especially considering the wider band gap of our material, which should result in a few percentage points of absolute efficiency drop with respect to a 1.55-eV material (*35*). Importantly for tandem solar cells, this 1.74-eV material appears to be capable of generating a higher V_{OC} than the 1.55-eV triiodide perovskites in planar heterojunction solar cells. Following Rau *et al.* (*36*), from the integration of the EQE over the blackbody radiation spectrum, we estimate the maximum attainable V_{OC} for our $FA_{0.83}Cs_{0.17}Pb(I_{0.6}Br_{0.4})_3$ device to be 1.42 V (details shown in fig. S15), which is 100 mV higher than that estimated for $MAPbI_3$ devices by Tvingstedt *et al.* and Tress *et al.* (*30*, *34*).

In order to demonstrate the potential impact of using this new perovskite composition in a tandem architecture, we fabricated semitransparent perovskite solar cells by sputter-coating indium tin oxide (ITO) on top of the perovskite cells, with the additional inclusion of a thin "buffer layer" of solution-processed ITO nanoparticles between the spiro-OMeTAD and the ITO. The efficiency of the semi-transparent $FA_{0.83}Cs_{0.17}Pb(I_{0.6}Br_{0.4})_3$ solar cells is 15.1%, as determined by the *I-V* curve, with a stabilized power output of 12.5%. Because the J_{SC} is similar to that of the cell with the Ag electrode, we expect that the slight drop in V_{OC} and SPO will be surmountable by better optimization of the ITO sputter-deposition procedure and buffer layer. We measured a Si heterojunction (SHJ) cell, with and without a semi-transparent perovskite cell held in front of it, and determined an efficiency of 7.3% filtered and 19.2% when uncovered. These results demonstrate the feasibility of obtaining a combined tandem solar cell efficiency ranging from 19.8%, if we combine with the stabilized power output of the semi-transparent cell, to 25.2% if we combine with the highest current density–voltage (*J-V*) measured efficiency of the $FA_{0.83}Cs_{0.17}Pb(I_{0.6}Br_{0.4})_3$ cell. Considering further minor improvements in the perovskite, optical management and integration, and choice of Si rear cell, it is feasible that this system could deliver up to 30% efficiency. In addition, this monotonic tunability of the band gap across the visible spectrum, without the complications of a structural phase transition will have direct impact on the color tunability and optimization of perovskites for light-emitting applications.

REFERENCES AND NOTES

1. V. Sivaram, S. D. Stranks, H. J. Snaith, *Sci. Am.* **313**, 54–59 (2015).
2. M. A. Green, K. Emery, Y. Hishikawa, W. Warta, E. D. Dunlop, *Prog. Photovolt. Res. Appl.* **23**, 805–812 (2015).
3. A. Shah, P. Torres, R. Tscharner, N. Wyrsch, H. Keppner, *Science* **285**, 692–698 (1999).
4. C. R. Kagan, D. B. Mitzi, C. D. Dimitrakopoulos, *Science* **286**, 945–947 (1999).
5. A. Kojima, K. Teshima, Y. Shirai, T. Miyasaka, *Priv. Commun.* **1**, 1 (2009).
6. M. M. Lee, J. Teuscher, T. Miyasaka, T. N. Murakami, H. J. Snaith, *Science* **338**, 643–647 (2012).
7. M. Liu, M. B. Johnston, H. J. Snaith, *Nature* **501**, 395–398 (2013).
8. J. Burschka *et al.*, *Nature* **499**, 316–319 (2013).
9. M. Green, A. Ho-Baillie, H. J. Snaith, *Nat. Photonics* **8**, 506–514 (2014).
10. N. J. Jeon *et al.*, *Nat. Mater.* **13**, 897–903 (2014).
11. N. J. Jeon *et al.*, *Nature* **517**, 476–480 (2015).
12. J. H. Noh, S. H. Im, J. H. Heo, T. N. Mandal, S. I. Seok, *Nano Lett.* **13**, 1764–1769 (2013).
13. G. E. Eperon *et al.*, *Energy Environ. Sci.* **7**, 982 (2014).
14. W. S. Yang *et al.*, *Science* **348**, 1234–1237 (2015).
15. E. T. Hoke *et al.*, *Chem. Sci.* **6**, 613–617 (2015).
16. B. Conings *et al.*, *Adv. Energy Mater.* 10.1002/aenm.201500477 (2015).
17. W. Rehman *et al.*, *Adv. Mater.* **27**, 7938–7944 (2015).
18. C. D. Bailie *et al.*, *Energy Environ. Sci.* **8**, 956–963 (2015).
19. P. Löper *et al.*, *Phys. Chem. Chem. Phys.* **17**, 1619–1629 (2015).
20. S. Albrecht *et al.*, *Energy Environ. Sci.* 10.1039/C5EE02965A (2015).
21. A. Binek, F. C. Hanusch, P. Docampo, T. Bein, *J. Phys. Chem. Lett.* **6**, 1249–1253 (2015).
22. S. Pang *et al.*, *Chem. Mater.* **26**, 1485–1491 (2014).
23. C. C. Stoumpos, C. D. Malliakas, M. G. Kanatzidis, *Inorg. Chem.* **52**, 9019–9038 (2013).
24. N. Pellet *et al.*, *Angew. Chem. Int. Ed. Engl.* **53**, 3151–3157 (2014).
25. S. D. Stranks, H. J. Snaith, *Nat. Nanotechnol.* **10**, 391–402 (2015).
26. J.-W. Lee *et al.*, *Adv. Energy Mater.* 10.1002/aenm.201501310 (2015).
27. H. Choi *et al.*, *Nano Energy* **7**, 80–85 (2014).

28. See the supplementary materials on *Science* Online.
29. C. Bi, Y. Yuan, Y. Fang, J. Huang, *Adv. Energy Mater.* 10.1002/aenm.201401616 (2014).
30. K. Tvingstedt *et al.*, *Sci. Rep.* **4**, 6071 (2014).
31. S. De Wolf *et al.*, *J. Phys. Chem. Lett.* **5**, 1035–1039 (2014).
32. A. Sadhanala *et al.*, *J. Phys. Chem. Lett.* **5**, 2501–2505 (2014).
33. R. L. Milot, G. E. Eperon, H. J. Snaith, M. B. Johnston, L. M. Herz, *Adv. Funct. Mater.* **25**, 6218–6227 (2015).
34. W. Tress *et al.*, *Adv. Energy Mater.* 10.1002/aenm.201400812 (2014).
35. H. J. Snaith, *Adv. Funct. Mater.* **20**, 13–19 (2010).
36. U. Rau, *Phys. Rev. B* **76**, 085303 (2007).
37. L. Mazzarella *et al.*, *Appl. Phys. Lett.* **106**, 023902 (2015).

ACKNOWLEDGMENTS

This project was funded in part by the Engineering and Physical Sciences Research Council through the Supergen Solar Energy Hub SuperSolar (EP/M024881/1, EP/M014797/1) and the European Research Council through the Stg-2011 Hybrid Photovoltaic Energy Relays and the European Union Seventh Framework Programme (FP7/2007-2013) under grant agreement 604032 of the MESO project, and the U.S. Office of Naval Research. M.H. is funded by Oxford PV Ltd. W.R. is supported by the Hans-Boeckler-Foundation. We thank our colleagues from the Centre For Renewable Energy Technologies Photovoltaic Measurement and Testing Laboratory, Loughborough University, for their contributions to the measurements of the semi-transparent devices. We also thank K. Jacob and M. Wittig [Helmholtz-Zentrum Berlin (HZB), Institute for Silicon Photovoltaics], L. Mazzarella, and S. Kirner (HZB, Institute PVcomB) for their contributions to fabricating the SHJ cell. The University of Oxford has filed a patent related to this work. The project was designed and conceptualized by D.M. and H.J.S. D.M. performed experiments, analyzed data, and wrote the first draft of the paper. G.S. fabricated and measured devices with semi-transparent electrodes. W.R. characterized the material using THz spectroscopy. G.E. helped with the experimental work and provided technical feedback on the writing of the paper. M.S. provided input and technical direction on the FA/Cs cation mixture. M.H. performed simulations for the optical modeling and calculated the maximum achievable V_{OC}. A.H. analyzed XRD data. N.S. provided input on the preparation of thin films using chemical bath depositions. L.K. and B.R. designed and supervised the fabrication of the SHJ cells. M.J. performed and analyzed EQE measurements. L.H. supervised and analyzed the THz spectroscopy measurements. H.J.S. supervised the overall conception and design of this project. All authors contributed to the writing of the paper.

SUPPLEMENTARY MATERIALS

www.sciencemag.org/content/351/6269/151/suppl/DC1
Materials and Methods
Supplementary Text
Figs. S1 to S15
References (*38*–*42*)

5 October 2015; accepted 3 December 2015
10.1126/science.aad5845

FOREST ECOLOGY

Dominance of the suppressed: Power-law size structure in tropical forests

C. E. Farrior,[1,2]* S. A. Bohlman,[3,4] S. Hubbell,[4,5] S. W. Pacala[6]

Tropical tree size distributions are remarkably consistent despite differences in the environments that support them. With data analysis and theory, we found a simple and biologically intuitive hypothesis to explain this property, which is the foundation of forest dynamics modeling and carbon storage estimates. After a disturbance, new individuals in the forest gap grow quickly in full sun until they begin to overtop one another. The two-dimensional space-filling of the growing crowns of the tallest individuals relegates a group of losing, slow-growing individuals to the understory. Those left in the understory follow a power-law size distribution, the scaling of which depends on only the crown area–to–diameter allometry exponent: a well-conserved value across tropical forests.

Tree size distributions—the frequency of trees by size—are important emergent properties of forests. Tree size distributions signal community-level interactions, are a critical diagnostic of the accuracy of scaling in mechanistic models, and are the basis of many aboveground forest carbon estimates (*1*–*3*). Despite differences in the tree vital rates that determine them, tropical forests worldwide have tree size distributions that follow tight power functions with very similar scaling for a wide range of diameters and commonly have deviations in the tails (*4*, *5*) (Fig. 1). Such a consistent emergent pattern begs an explanation, one that is likely to provide an important key to understanding the mechanisms governing tropical forest dynamics (*6*).

Current theories explaining the consistency of tropical forest size structure are controversial. Explanations based on scaling up individual metabolic rates (*4*, *7*, *8*) are criticized for ignoring the importance of asymmetric competition for light in causing variation in dynamic rates (*9*–*11*). Other theories, which embrace competition and scale individual tree vital rates through an assumption of demographic equilibrium (*5*, *10*, *12*, *13*), are criticized for lacking parsimony, because predictions rely on site-level, size-specific parameterizations (*14*). Despite their differences, common to these theories is the notion that the predicted size structure is a property of steady-state forests far removed from the influence of disturbance. We tested this prediction. We explored the size structure within a well-studied tropical forest and, with theoretical corroboration, present a parsimonious and biologically intuitive explanation for the power-function size structure, observed deviations, and the consistency of the scaling across forests.

[1]National Institute for Mathematical and Biological Synthesis, Knoxville, TN 37996, USA. [2]Department of Integrative Biology, University of Texas at Austin, Austin, TX 78712, USA. [3]School of Forest Resources and Conservation, University of Florida, Gainesville, FL 32611, USA. [4]Smithsonian Tropical Research Institute, Apartado 0843–03092, Balboa, Ancon, Republic of Panama. [5]Department of Ecology and Evolutionary Biology, University of California, Los Angeles, CA 90095, USA. [6]Department of Ecology and Evolutionary Biology, Princeton University, Princeton, NJ 08544, USA.
***Corresponding author. E-mail: cfarrior@nimbios.org**

We explored temporal and spatial patterns in tropical forest size structure in 50 ha and 30 years of data from Barro Colorado Island, Panama (BCI) (*15*–*17*). Forest patches in the early stages of recovery from small-scale disturbances (*18*) develop a power function that extends through a greater range of diameters as time progresses (Fig. 2). At 25 to 30 years after disturbance, the power function extends through the full range of diameters present, and unlike in younger patches, a power law is a likely model of the data [(*18*), criteria following (*19*)]. However, the power-law fit is again lost in patches with more than 30 years since the last disturbance.

Having reached the limit of our temporal analyses, we examined forest patches as grouped by forest size. We used the metric D^*_{est} as an estimate of the size threshold for tree canopy status in a patch (*18*). For each range of D^*_{est}, we fit a power function (with the same scaling as Fig. 1, fit to all data) that transitions at a single size class to an exponential distribution (Fig. 3A) (*18*). This best-fit size class of transition increases with D^*_{est} (Fig. 3B, $P = 0.005$, t test, R-squared = 0.76,

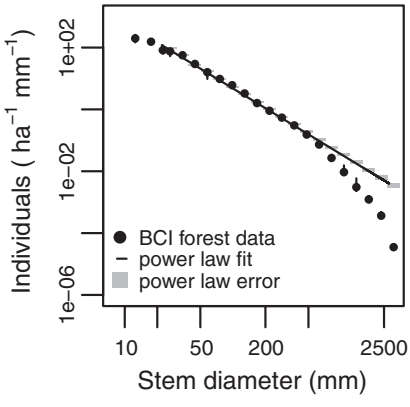

Fig. 1. Size distribution of the 50-ha tropical forest dynamics plot on BCI. The average (points) and range (bars) by size class among all seven censuses are shown. The best-fit power law distribution to all diameters from censuses 3 to 7 (*18*) is drawn (black line). The expected range of variation for that power law, given the average census sample size by size class, is in gray [95% range (*18*)].